

NeXtQSM - A complete deep learning pipeline for data-consistent quantitative susceptibility mapping trained with hybrid data *

Francesco Cognolato^{1,2}, Kieran O'Brien^{2,4}, Jin Jin^{2,4}, Simon Robinson^{1,5,6,7}, Frederik B. Laun⁸, Markus Barth^{1,2,3}, and Steffen Bollmann^{1,2,3}

¹ Centre for Advanced Imaging, The University of Queensland, Brisbane, Australia

² ARC Training Centre for Innovation in Biomedical Imaging Technology, The University of Queensland, Brisbane, Australia

³ School of Information Technology and Electrical Engineering, The University of Queensland, Brisbane, Australia

⁴ Siemens Healthcare Pty Ltd, Brisbane, Queensland, Australia

⁵ High Field MR Center, Department of Biomedical Imaging and Image-Guided Therapy, Medical University of Vienna, Vienna, Austria

⁶ Department of Neurology, Medical University of Graz, Graz, Austria

⁷ Karl Landsteiner Institute for Clinical Molecular MR in Musculoskeletal Imaging, Vienna, Austria

⁸ Institute of Radiology, University Hospital Erlangen, Friedrich-Alexander-Universität Erlangen-Nürnberg (FAU), Erlangen, Germany

Abstract. Deep learning based Quantitative Susceptibility Mapping (QSM) has shown great potential in recent years, outperforming traditional non-learning approaches in speed and accuracy. However, many of the current deep learning approaches are not data consistent, require in vivo training data or do not solve all steps of the QSM processing pipeline. Here we aim to overcome these limitations and developed a framework to solve the QSM processing steps jointly. We developed a new hybrid training data generation method that enables the end-to-end training for solving background field correction and dipole inversion in a data-consistent fashion using a variational network that combines the QSM model term and a learned regularizer. We demonstrate that NeXtQSM overcomes the limitations of previous model-agnostic deep learning methods and show that NeXtQSM offers a complete deep learning based pipeline for computing robust, fast and accurate quantitative susceptibility maps.

Keywords: Magnetic Susceptibility · Data-consistent Deep Learning · Electromagnetic Tissue Properties · Simulated Training Data

1 Introduction

Quantitative Susceptibility Mapping (QSM) is a Magnetic Resonance Imaging (MRI) technique which has gained a lot of attention in the last decade because

* The source code will be provided upon request.

of its potential to extract in vivo magnetic susceptibilities [9,44,46]. The quantitative information contained in each voxel linearly reflects the tissue magnetic susceptibility. As a result, QSM is able to reveal information about iron concentrations in the gray matter [2,48,26,43,57,49,23], demyelinating lesions in the white matter [53,55,23], copper accumulation [15], blood oxygenation [12], microbleeds [32] and differentiates them from microcalcifications [42]. Alterations of these susceptibilities can be linked to ageing [2] as well as neurological diseases such as Parkinson’s disease [3,25], Alzheimer’s disease [4], Huntington’s disease [48] and multiple sclerosis [11,54,60].

The extraction of tissue susceptibilities requires multiple steps in a processing pipeline starting from the phase signal of a gradient-recalled echo (GRE) sequence and includes phase unwrapping, background field removal and dipole inversion. The first step, phase unwrapping is commonly solved by either region-growing [17], Laplacian-based [41] or path-based [1,10] algorithms. The next step in the QSM pipeline, the so-called background field removal, can be solved using Sophisticated Harmonic Artifact Reduction for Phase data (SHARP) [43] and its extensions [27,62,47] or with Laplacian-based [61] algorithms (for a review see: [44]). The final step, the so-called dipole inversion, extracts the susceptibility values and requires the solution of an ill-posed inverse problem. The dipole inversion aims to spatially de-convolve the result of a forward operation, which consists of a point-wise multiplication in Fourier domain between the dipole kernel and the object. Deconvolution in Fourier space would be a division by the dipole kernel, but the kernel contains zeros and it is therefore not possible to directly perform the inverse operation and would lead to the amplification of noise. One solution proposed to overcome the ill-posed problem is known as “Calculation of susceptibility through multiple orientation sampling” (COSMOS) [31,51] which requires at least three different orientations to eliminate the singularities in the dipole operation. Despite the high quality of the COSMOS reconstruction, this method is not practical because of its long acquisition time and requiring the acquisition of the object in differing rotations.

Due to the impracticability of COSMOS, single orientation solutions have been proposed for phase images. A first group of solutions, named inverse filtering, include “Truncated k-space division” (TKD) [52] and “Superfast Dipole Inversion” (SDI) [45], methods which use modifications of the dipole kernel whose small values are directly replaced by a constant value. This leads to solutions with reduced streaking artifacts but the resultant magnetic susceptibility values are systematically underestimated and there is no universal way of robustly defining the value of this constant due to its dependence on the noise level in the data.

A second group of solutions can be regarded as iterative methods which are based on the minimization of the L1 or L2 norms between the measured magnetic field and the field generated by convolving the dipole with the magnetic susceptibility distribution using standard optimization techniques (conjugate gradient,

steepest descent). These techniques can also include prior information as a regularization term based on the underlying anatomical structure, for instance “Morphology Enabled Dipole Inversion” (MEDI) [30], or sparsity assumptions. These traditional methods require a careful hyperparameter tuning, can take a long time to reconstruct and generate over-smooth or piece-wise constant solutions depending on the regularizers applied.

The recent advent and huge improvements in deep learning techniques in computer vision [39] led to an application of these methods to multiple problems in MRI and have shown effectiveness in solving QSM problems such as background field removal [6,29] and dipole inversion [7,58,8,22,16] (for a review see: [19]).

However, a limitation of the current state-of-the-art techniques is that the background field correction and dipole inversion are either treated as two independent problems (e.g. [13] does not include background field correction), leading to accumulations of errors between consecutive steps, or do not include a dipole inversion that delivers data consistent solutions (e.g. [50]).

Due to the fact that these steps are mostly treated independently, any imprecision or inaccuracies can propagate to the next step affecting the final reconstruction. One traditional and well-established algorithm (TGV-QSM, [24]) solves both problems in a single optimization procedure but requires substantial amounts of compute time due to the difficult variational optimization problem (solved by employing general primal-dual algorithms for finding saddle points for convex-concave problems). Another traditional solution is the total field inversion [20] that aims to invert all sources.

Some deep learning methods have been proposed that combine the dipole inversion and background field correction [50,28], but these models do not incorporate data-consistency constraints in the dipole inversion. Achieving a data consistent solution would make the reconstruction more robust and invariant to the dipole kernel magnetic field direction and has been shown to be a beneficial post-processing step for deep learning solutions [59]. In addition, most current deep learning QSM techniques require in vivo training data and often use COSMOS [31] as a target, which can only be obtained by multi orientation measurements and is not a realistic target for a single orientation measurement. To address these limitations, we propose variational NEural network trained on complex realistic structures for Quantitative Susceptibility Mapping (NeXtQSM), an end-to-end deep learning pipeline trained on hybrid data to solve the background field correction and dipole inversion in a data consistent fashion composed by two models which are trained together to solve the two processing steps jointly. Our study is evaluated on the QSM reconstruction challenge 2016 [35] and on in vivo 7T data.

2 Theory

2.1 QSM forward operation

The QSM physical model operation is generally described by the equation $Y = \Phi X + \epsilon$, where X is the object in Fourier space containing the susceptibility values, ϵ the noise during the measurement, Y the measured local field and the forward operation $\Phi = F^{-1}DF$ which is a convolution operation with the dipole kernel in Image domain.

For numerical efficiency, the convolution operation is commonly calculated in Fourier domain F as a pointwise multiplication. The dipole kernel in Fourier space for magnetic fields [40] in the z-axis can be represented with the following equation:

$$D = \frac{1}{3} - \frac{k_z^2}{k_x^2 + k_y^2 + k_z^2} \quad (1)$$

where k_x , k_y and k_z are the k-space values in the respective directions. When the k-space values fraction approaches 1/3, the dipole kernel results to 0, making the dipole inversion ill-posed.

2.2 Variational Networks

These sophisticated models are the bridge connecting traditional variational methods and deep learning. In variational methods, the solution of inverse problems can be formulated as an iterative process where at each iteration an objective function $E(x)$ composed by two different terms is minimized:

$$\min_x E(x) = \lambda \underbrace{\|Y - \Phi x\|_2^2}_{f(x)} + \Psi(x) \quad (2)$$

where $f(x)$ is the data consistency term, in this specific case containing the QSM forward model Φ , which helps in applying the model to a variety of input data that would lead to unstable solutions in model-agnostic deep learning solutions, $\Psi(x)$ is the regularizer or prior knowledge which prevents overfitting on the data and λ is the learnable trade-off factor between data term and regularizer.

In traditional variational methods, a hand-crafted prior term Ψ such as Total Variation [36] is chosen, whereas in variational networks, which can be considered as iterative hybrid methods, the regularizer is learned using convolutional neural networks.

At the end of the prefixed number of iterations, a final reconstruction error E_{recon} is calculated:

$$E_{recon} = \sum_{n=0}^N \frac{1}{N} \|\hat{x}_S - X\|_2^2; \quad (3)$$

where \hat{x}_S is the reconstructed susceptibility map, X is the actual ground truth susceptibility values obtained from the hybrid structures and N the number of samples considered in the batch. Through the minimization of this error, the weights of the convolutional neural networks at each step are optimized.

Our pipeline (Fig. 1) learns from realistic simulations of the physical properties of the problems and complex realistic structures which are synthetically created from segmentation maps. The framework is composed of two deep learning architectures trained together in an end-to-end fashion for solving background field removal and dipole inversion. The model solving the background field removal is a standard fully convolutional U-Net [38], whereas the dipole inversion is achieved by a Variational Network [21,22].

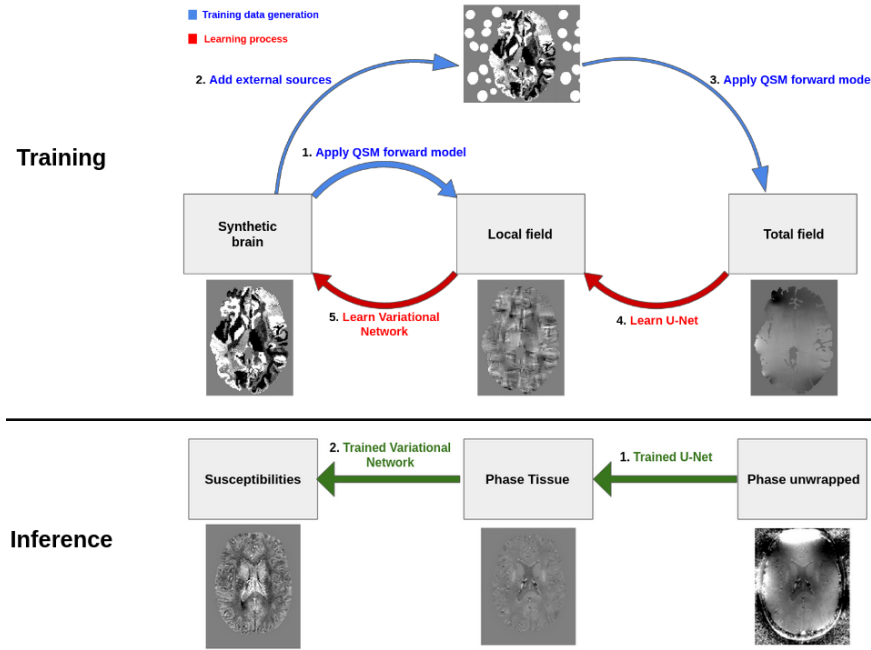


Fig. 1. Illustration of the NeXtQSM pipeline for training (top) and inference time (bottom). The training includes both the training data generation process (blue) and the two deep learning models trained jointly in one optimization (red). In the training data generation (blue), we apply the QSM forward operation to the segmented brains with and without external sources to yield the data for the two learning steps. During training (red), the two architectures are trained in an end-to-end fashion. At inference time (green), the trained models perform the prediction from the unwrapped phase data to the magnetic susceptibility maps.

2.3 Training data

Due to the lack of a realistic ground truth susceptibilities for the dipole inversion and the fact that deep learning techniques need to be trained on fairly large amounts of data to be able to generalize, both of our two models were entirely trained with simulated hybrid data.

The hybrid data are based on the deformation of segmented brain MRI scans using affine transformations and a Gaussian Mixture Model [5], which substituted the class labels with randomly sampled intensities from a prior distribution (Fig. 2).

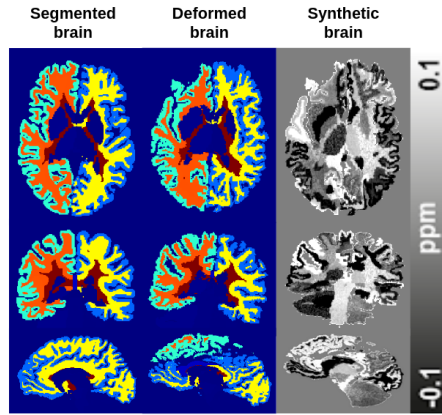


Fig. 2. Visual illustration of the hybrid training data generation. The left column shows the input segmentation map, the center the deformed brain and on the right the results of the random sampling by class using a Gaussian Mixture Model.

The hybrid data were generated from 28 participants (21 to 34 years of age, average of 26.5 years, 14 males) acquired on a 3 T whole-body MRI scanner (Siemens Healthcare, Erlangen, Germany). The MP2RAGE [33] scans (matrix = $240 \times 256 \times 176$, resolution = 1 mm isotropic, GRAPPA = 3, TR = 4000 ms, TE = 2.89 ms, TI1/TI2 = 700/2220 ms) were segmented in 184 classes using FreeSurfer v6 [14]. For each of the 28 healthy individuals, 30 deformed hybrid brains were created with different simulated susceptibility values per region drawing from the initially described normal distribution, for a total of 840 hybrid brains, and used for the final training. We tested larger amounts of deformed hybrid brains per individual, but did not see any further training improvements with more augmentation. After randomly sampling the intensities per segmentation class, each brain dataset was scaled to have 0 mean with a normal distribution whose 1st quartile was set around -0.5 and the 3rd at 0.5.

As shown in the pipeline (Fig. 1), the training data generation consisted of one part for the dipole inversion and one for the background field removal (local field and total field respectively in Fig. 4). The dipole inversion training data were generated applying the QSM forward operation to the hybrid brains. For the background field removal problem, a random number of around 100 elliptical external sources (Fig. 3), simulating large susceptibility sources such as air (susceptibility value around 9.2 ppm), whose size is randomly sampled around one-tenth of the brain volume. The simulated background field sources were placed randomly around the synthetic brain before convolving it with the QSM forward model (Fig. 1 and 3).

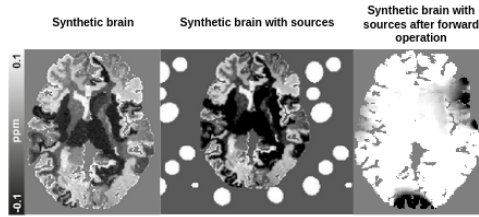


Fig. 3. Illustration of the data generation for the background field removal part. Elliptical sources were randomly placed around the brain, and, after applying the QSM forward model, the background was masked out, leaving only the brain with the effect of the external sources.

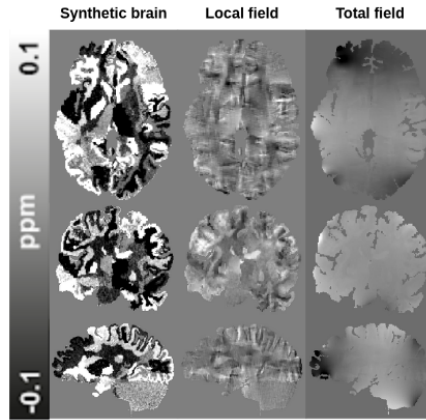


Fig. 4. Illustration of the training dataset. The left column shows the initial hybrid brain with simulated susceptibility values, the center shows the data after application of the QSM dipole model and on the right the data after applying the forward model including the effect of external sources.

2.4 Pipeline architecture

The first learning block (number 4 in Fig. 1) of the pipeline has the aim to remove background magnetic field contributions from sources which are external to the object during the MR measurement. In particular, this stage used a fully convolutional neural network, the well-known U-Net [38], to predict the local field using a feed-forward operation given the total field.

The second stage used a Variational Network [22,21] to enable a data-consistent solution of the QSM dipole inversion. The learned variational network regularizers are implemented using the U-Net architecture [38] at each step. The CNN architecture adjusts its weights during training so that it helps the convergence of the reconstructed volume through a trade-off with the data term. A detailed description of the layers contained in the two architectures is provided in Fig. 5. Each CNN block is composed of standard convolutional operations with Leaky Relu [56] activation functions.

U-Net : Background field removal		Variational Network Prior : Dipole inversion	
Layer name	Output shape	Layer name	Output shape
Input	(192, 192, 192, 1)	Input	(192, 192, 192, 1)
Encoder CNN Block 1	(192, 192, 192, 16)	Encoder CNN Block 1	(192, 192, 192, 16)
Encoder CNN Block 2	(96, 96, 96, 32)	Encoder CNN Block 2	(96, 96, 96, 32)
Encoder CNN Block 3	(48, 48, 48, 64)	Decoder CNN Block 1 \oplus E1	(192, 192, 192, 32)
Encoder CNN Block 4	(24, 24, 24, 128)	Final	(192, 192, 192, 1)
Encoder CNN Block 5	(12, 12, 12, 256)		
Encoder CNN Block 6	(6, 6, 6, 512)		
Decoder CNN Block 1 \oplus E5	(12, 12, 12, 512)		
Decoder CNN Block 2 \oplus E4	(24, 24, 24, 256)		
Decoder CNN Block 3 \oplus E3	(48, 48, 48, 128)		
Decoder CNN Block 4 \oplus E2	(96, 96, 96, 64)		
Decoder CNN Block 5 \oplus E1	(192, 192, 192, 32)		
Final	(192, 192, 192, 1)		

Fig. 5. Detailed illustration of the different layers composing the two networks which will be trained end-to-end.

2.5 Training procedure

The training was done in an end-to-end fashion, on both the background field and dipole inversion architectures jointly after having trained them separately on our hybrid dataset. At each training epoch, 840 hybrid brains were used to learn the problem. The workflow of a training step can be found in Algorithm 1 and is visually illustrated in Fig. 6.

Our end-to-end pipeline was implemented using Tensorflow 2.3.0 and trained for 48 hours on a single NVIDIA Tesla V100 32GB GPU with batch size 2. Despite the small batch size, after initial tests we decided to not divide the volumes into smaller 3D patches and fed the complete dataset into the network to better represent the total field to the network architecture.

The end-to-end pipeline was trained for 50 epochs and optimized using Adam

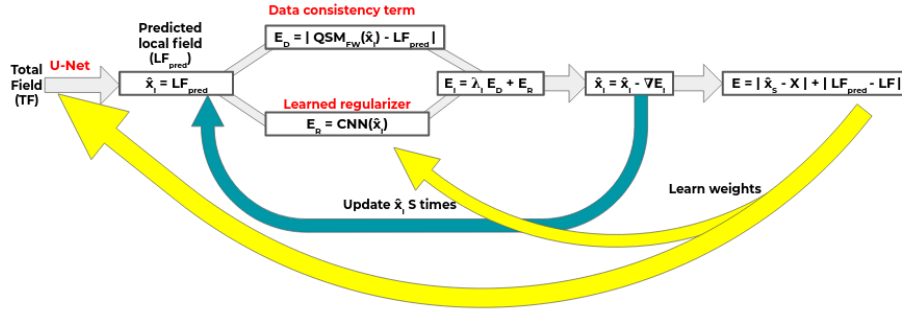


Fig. 6. Graphical description of a training step. The Variational Network loss function is composed of two parts, a data consistency and a regularizer term. X is the hybrid brain, TF total field, LF local field, LF_{pred} the predicted local field, S iterative steps, λ trade-off term, Ψ_i NeuralNet at step i , \hat{x}_S reconstructed volume after S steps. Moreover, the backpropagation procedure is indicated by a yellow arrow which updates the weights of both the U-Net for the background field removal and the regularizer of the variational network.

optimizer with learning rate $4e-4$ and betas set to 0.9 and 0.999 .

Our end-to-end deep learning pipeline to solve background field removal and dipole inversion was compared both quantitatively on metrics and visually to other methods which offer the solution of these two QSM steps together, specifically we compare NeXtQSM to both learning (such as SHARQnet [6] followed by DeepQSM [7]) and non-learning approaches (such as TGV-QSM [24] and STI-Suite (VSHARP + iLSQR)) using their default parameters.

We tested these methods on datasets from the QSM Challenge 2016 [35] and on in vivo 7T data of a 27 year old male participant. The 7T data were acquired using a multiple echo time gradient-recalled echo (GRE) 3D whole-brain data sets: repetition time (TR) = 25 ms, echo time (TE) = 4.4, 7.25, 10.2, 13.25, 16.4, 19.65, 23 ms, flip angle = 13° , field of view (FOV) = $210 \times 181.5 \times 120 \text{ mm}^3$, matrix = $280 \times 242 \times 160$ (0.75 mm isotropic voxels), parallel imaging (generalized autocalibrating partially parallel acquisitions (GRAPPA), acceleration factor = 2, 24 autocalibration lines), monopolar readout gradient, symmetric echo, 1116 Hz/pixel, first echo flow compensated, acquisition time (TA) = 7.9min. For combining the individual channels we utilized the COMPOSER method [37] with the first echo of a GRE scan (3D GRE with TR = 8 ms, three echoes TE = 1.02, 3.06, 6.12 ms, flip angle = 5° , FOV = $245 \times 245 \times 182 \text{ mm}^3$, matrix = $70 \times 70 \times 52$ (3.5-mm isotropic voxels), monopolar readout gradient, symmetric echo, 1211 Hz/pixel, TA = 24 s) and we used the first echo of this 7T dataset in the QSM processing. A brain mask was generated using the brain extraction tool BET from FSL [18].

Algorithm 1: NeXtQSM end-to-end training step. X is hybrid brain, TF total field, LF local field, LF_{pred} the predicted local field, S iterative steps, λ trade-off term, Ψ_i NeuralNet at step i , N batch size, \hat{x}_S reconstructed volume after S steps. The arrows indicate the assignment to a new variable.

```

 $LF_{pred} \leftarrow UNet(TF)$ 
 $\hat{x}_i \leftarrow LF_{pred}$ 
for  $i < S$  do
   $f(\hat{x}_i) \leftarrow \frac{\lambda_i}{N} \sum_{n=0}^N |LF_{pred} - \Phi \hat{x}_i| + \Psi_i(\hat{x}_i)$ 
   $\hat{x}_{i+1} \leftarrow \hat{x}_i - \frac{\partial f(\hat{x}_i)}{\partial \hat{x}_i}$ 
end
 $E_{recon} \leftarrow \frac{1}{N} \sum_{n=0}^N |\hat{x}_S - X| + |LF_{pred} - LF|$ 
min  $E_{recon}$ 

```

2.6 Metrics

In order to quantify the error between our and other established methods, we used the following metrics utilized in the 2019 QSM reconstruction challenge [34]:

- **NRMSE** (Normalized Residual Mean Squared Error) where the normalization is calculated with respect to the L2-norm of the provided ground truth method.
- **ddNRMSE** (demeaned detrended Normalized Residual Mean Squared Error) because some algorithms can produce underestimated results.
- **SSIM** (Structural SIMilarity) to quantify how different the structure of two volumes are.

Gaussian noise perturbations In order to test the robustness of our pipeline, we apply Gaussian Noise perturbations with 0 mean and 0.005 variance to a control participant dataset acquired at 7T, which is one of our testing datasets used in the results section.

3 Results

3.1 QSM Challenge 2016

The first experiment to evaluate the performance of the pipeline was performed on in vivo data provided by the QSM challenge 2016 [35]. Fig. 7 shows the final QSM reconstruction of NeXtQSM compared to alternative methods. In addition to the visual comparison, quantitative metrics have been computed with respect to COSMOS and shown in the table 1, but one should keep in mind that it is not feasible to achieve the same reconstruction quality using a single orientation. NeXtQSM is able to outperform all the other analyzed methods in most of the quantitative metrics used.

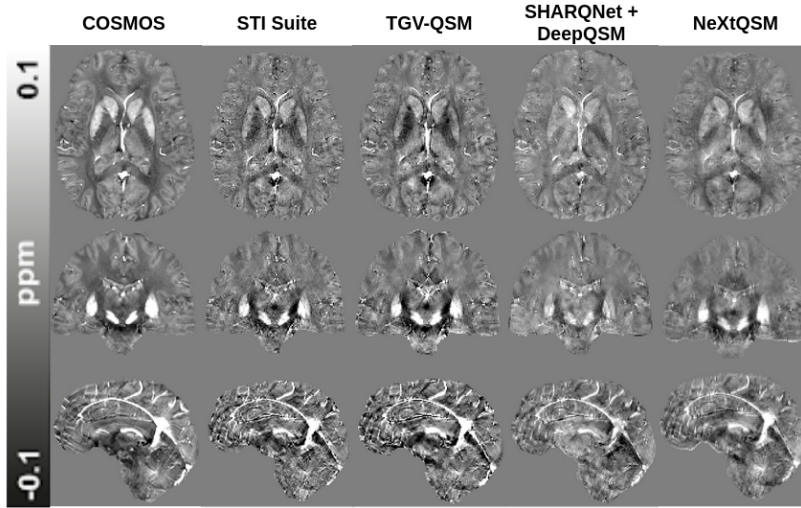


Fig. 7. Visual comparison of different methods using the QSM Challenge 2016 data. It can be observed that all methods deliver artifact-free QSM reconstructions, however SHARQnet + DeepQSM show reduced contrast in comparison to all other methods. STI Suite provides a noisier solution with respect to the other methods. The NeXtQSM solution has lower contrast, but more similar to the COSMOS method.

Table 1. Quantitative comparison of different methods using the QSM Challenge 2016 data. The newly proposed method NeXtQSM shows the best quantitative metrics for NRMSE and ddNRMSE and second best metric for SSIM.

Background field removal + Dipole inversion			
Method	NRMSE	ddNRMSE	SSIM
NeXtQSM	71.29	98.34	0.947
DeepQSM	91.01	170.15	0.918
TGV-QSM	90.67	113.09	0.939
STI Suite	82.47	113.49	0.948

3.2 Healthy subject dataset

A second experiment utilized a control participant dataset which is shown in Fig. 8 to show that our end-to-end pipeline is applicable to ultra-high field MRI data. The visual comparison indicates that NeXtQSM delivers a robust background field correction and dipole inversion similar to established QSM methods like TGV-QSM or STI Suite. It can also be observed that the model agnostic deep learning QSM method SHARQnet + DeepQSM suffers from a lack in contrast and shows residual background field artifacts.

Robustness to noise perturbations It can be observed in Fig. 9 that the data consistency constraint in NeXtQSM has a stabilising impact against Gaus-

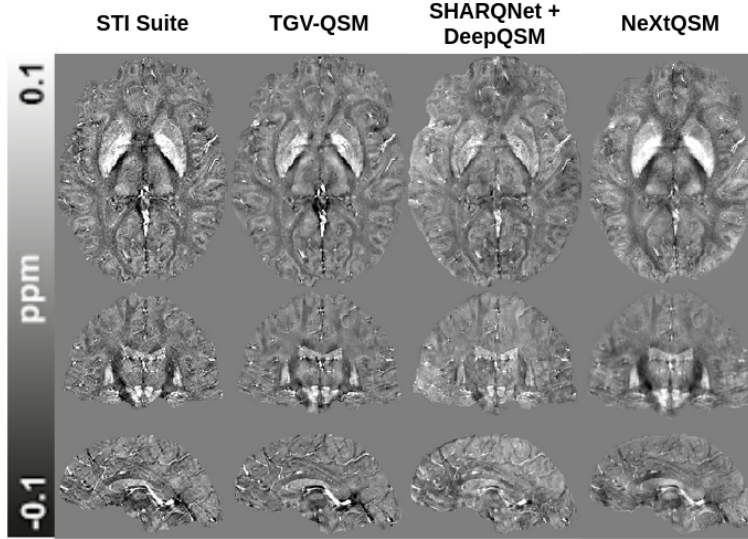


Fig. 8. Visual comparison of different methods using the 7 T control participant dataset. It can be observed that all methods deliver artifact free QSM reconstructions, but SHARQnet and DeepQSM show reduced contrast in comparison to the other methods.

sian noise perturbation especially in comparison to the model-agnostic approach SHARQnet + DeepQSM.

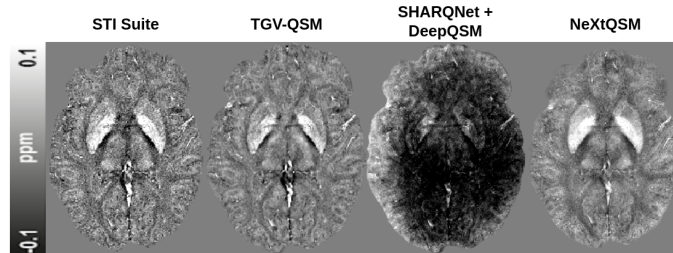


Fig. 9. Visual comparison of the robustness to Gaussian noise perturbations applied to the input. It can be seen that model-agnostic deep learning like SHARQnet and DeepQSM fail to be robust to a change in input data distribution.

We also measured the processing times of the different pipelines (tested on an Intel Core i5-10400 CPU) and the run-times range from 1500s for TGV-QSM [24], 450s for STI suite, 70s for SHARQnet [6] and DeepQSM [7] and 90s for NeXtQSM.

4 Discussion

The proposed NeXtQSM pipeline is capable of learning the background field correction and dipole inversion from hybrid training data. We show that the trained networks generalize well to in vivo data of the 2016 QSM challenge and a 7T ultra-high field MRI dataset. Comparing NeXtQSM to established QSM algorithms, both learning and non-learning based, indicates that our hybrid training data captures both the geometrical and physical properties needed to train deep learning models, learn the QSM dipole model and the effect of external sources on the brain causing the background field as well as generalize to in vivo data. Moreover, we found that training our pipeline end-to-end delivered accurate and robust results. The data consistency constraint helps in increasing the robustness of the processing to noise.

In contrast to existing model agnostic deep learning QSM solutions, our framework includes a data consistency constraint for the dipole inversion implemented via a variational network. This increased robustness can be seen for example via a perturbation with Gaussian Noise of the input data resulting in unusable results for a model agnostic deep learning methods, such as DeepQSM and SHARQnet (see Fig. 9).

Moreover, we found that training NeXtQSM with larger patches was beneficial and in the final version decided against a training regime that would split-up the brain-volumes in sub-patches at all as proposed in earlier works [8,7,6]. Due to progress in the available GPU hardware we managed to train NeXtQSM with the complete brain volume and a small batch-size. This training is better in line with the theoretical concepts of QSM and especially the background field correction profits from a "complete picture" of the artifacts caused by external sources, like air-tissue interfaces.

Although other deep learning approaches have previously attempted to solve the background field removal and dipole inversion in one step [50,28], these methods use model-agnostic deep learning approaches, which are very sensitive to slight perturbations in the input data. Moreover, the training data are not generated from the actual physical model utilizing hybrid data, but they are generated from established traditional methods and acquired in vivo datasets limiting the possible accuracy.

NeXtQSM elegantly combines the advantages of deep learning and classical QSM inversion techniques: Model agnostic deep learning techniques deliver very fast and high fidelity QSM solutions but do not include the data consistency constraint and can therefore be very sensitive to data distribution changes. Traditional approaches like TGV-QSM [24] deliver data consistent solutions, but the optimization process is computationally expensive and therefore fairly slow, limiting potential clinical applications. NeXtQSM is substantially faster (90 s) than traditional techniques (1500 s for TGV QSM and 450 s for STI-Suite) and more

robust to input data variations than model agnostic deep learning approaches.

To yield quantitative metrics, we compared the NeXtQSM performance to the COSMOS reconstruction provided by the 2016 reconstruction challenge. However, it is important to note that this "ground truth" is computed using multiple orientations requiring very long acquisition times that makes COSMOS not suitable for patient studies, whereas NeXtQSM requires only one orientation for reconstructing the susceptibility map.

5 Conclusion

In this study, we presented NeXtQSM, a complete deep learning pipeline trained only on hybrid samples to solve QSM's background field and dipole inversion steps in a data-consistent fashion. Our approach is more robust to variations in the input data than model agnostic deep learning methods, but substantially faster than traditional QSM techniques.

Acknowledgments

The authors acknowledge the facilities and scientific and technical assistance of the National Imaging Facility, a National Collaborative Research Infrastructure Strategy (NCRIS) capability, at the Centre for Advanced Imaging, the University of Queensland. This research was undertaken with the assistance of resources and services from the Queensland Cyber Infrastructure Foundation (QCIF). Oracle for Research provided Oracle Cloud credits and related resources to support this project. MB acknowledges funding from Australian Research Council Future Fellowship grant FT140100865. SR was supported by the Marie Skłodowska-Curie Action (MS-fMRI-QSM 794298). This research was funded (partially or fully) by the Australian Government through the Australian Research Council (project number IC170100035). Funding for the position of F.B.L. by the German Research Foundation is gratefully acknowledged (LA 2804/12-1).

References

1. Hussein S. Abdul-Rahman, Munther A. Gdeisat, David R. Burton, Michael J. Lalor, Francis Lilley, and Christopher J. Moore. Fast and robust three-dimensional best path phase unwrapping algorithm. *Appl. Opt.*, 46(26):6623–6635, Sep 2007.
2. Julio Acosta-Cabronero, Matthew J. Betts, Arturo Cardenas-Blanco, Shan Yang, and Peter J. Nestor. In Vivo MRI Mapping of Brain Iron Deposition across the Adult Lifespan. *Journal of Neuroscience*, 36(2):364–374, 2016.
3. Julio Acosta-Cabronero, Arturo Cardenas-Blanco, Matthew Betts, Michaela Butryn, Jose Valdes-Herrera, Imke Galazky, and Peter Nestor. The whole-brain pattern of magnetic susceptibility perturbations in Parkinson's disease. *Brain : a journal of neurology*, 140, 11 2016.

4. Julio Acosta-Cabronero, Guy B. Williams, Arturo Cardenas-Blanco, Robert J. Arnold, Victoria Lupson, and Peter J. Nestor. In Vivo Quantitative Susceptibility Mapping (QSM) in Alzheimer’s Disease. *PLOS ONE*, 8(11):1–15, 11 2013.
5. Benjamin Billot, Douglas Greve, Koen Van Leemput, Bruce Fischl, Juan Eugenio Iglesias, and Adrian V. Dalca. A Learning Strategy for Contrast-agnostic MRI Segmentation, 2020.
6. Steffen Bollmann, Matilde Holm Kristensen, Morten Skaarup Larsen, Mathias Vassard Olsen, Mads Jozwiak Pedersen, Lasse Riis Østergaard, Kieran O’Brien, Christian Langkammer, Amir Fazlollahi, and Markus Barth. SHARQnet – Sophisticated harmonic artifact reduction in quantitative susceptibility mapping using a deep convolutional neural network. *Zeitschrift für Medizinische Physik*, 29(2):139–149, 2019. Special Issue: Deep Learning in Medical Physics.
7. Steffen Bollmann, Kasper Gade Bøtker Rasmussen, Mads Kristensen, Rasmus Guldhammer Blendal, Lasse Riis Østergaard, Maciej Plochanski, Kieran O’Brien, Christian Langkammer, Andrew L. Janke, and Markus Barth. DeepQSM - Using deep learning to solve the dipole inversion for quantitative susceptibility mapping. *NeuroImage*, 195:373–383, 2019.
8. Yicheng Chen, Angela Jakary, Sivakami Avadiappan, Christopher P. Hess, and Janine M. Lupo. QSMGAN: Improved Quantitative Susceptibility Mapping using 3D Generative Adversarial Networks with Increased Receptive Field, 2019.
9. Andreas Deistung, Ferdinand Schweser, and Jürgen R. Reichenbach. Overview of quantitative susceptibility mapping. *NMR in Biomedicine*, 30(4):e3569, 2017. e3569 NBM-15-0326.R2.
10. Barbara Dymerska, Korbinian Eckstein, Beata Bachrata, Bernard Siow, Siegfried Trattng, Karin Shmueli, and Simon Robinson. Phase unwrapping with a rapid opensource minimum spanning tree algorithm (ROMEO). *Magnetic Resonance in Medicine*, 85, 10 2020.
11. Sarah Eskreis-Winkler, Kofi Deh, Ajay Gupta, Tian Liu, Cynthia Wisnieff, Moonsoo Jin, Susan Gauthier, Yi Wang, and Pascal Spincemaille. Multiple sclerosis lesion geometry in Quantitative Susceptibility Mapping (QSM) and phase imaging. *Journal of Magnetic Resonance Imaging*, 42, 08 2014.
12. Audrey Fan, Berkin Bilgic, Louis Gagnon, Thomas Witzel, Himanshu Bhat, Bruce Rosen, and Elfar Adalsteinsson. Quantitative Oxygenation Venography from MRI Phase. *Magnetic resonance in medicine : official journal of the Society of Magnetic Resonance in Medicine / Society of Magnetic Resonance in Medicine*, 72, 07 2014.
13. Ruimin Feng, Jiayi Zhao, He Wang, Baofeng Yang, Jie Feng, Yuting Shi, Ming Zhang, Chunlei Liu, Yuyao Zhang, Jie Zhuang, and Hongjiang Wei. MoDL-QSM: Model-based deep learning for quantitative susceptibility mapping. *NeuroImage*, 240:118376, October 2021.
14. Bruce Fischl, David H. Salat, Evelina Busa, Marilyn Albert, Megan Dieterich, Christian Haselgrove, Andre van der Kouwe, Ron Killiany, David Kennedy, Shuna Klaveness, Albert Montillo, Nikos Makris, Bruce Rosen, and Anders M. Dale. Whole Brain Segmentation: Automated Labeling of Neuroanatomical Structures in the Human Brain. *Neuron*, 33(3):341–355, 2002.
15. Dominik Fritzsche, Martin Reiss-Zimmermann, Robert Trampel, Robert Turner, Karl-Titus Hoffmann, and Andreas Schäfer. Seven-Tesla Magnetic Resonance Imaging in Wilson Disease Using Quantitative Susceptibility Mapping for Measurement of Copper Accumulation. *Investigative radiology*, 49, 11 2013.
16. Yang Gao, Xuanyu Zhu, Bradford A. Moffat, Rebecca Glarin, Alan H. Wilman, G. Bruce Pike, Stuart Crozier, Feng Liu, and Hongfu Sun. xQSM: quantitative

- susceptibility mapping with octave convolutional and noise-regularized neural networks. *NMR in Biomedicine*, 34(3), Dec 2020.
17. Mark Jenkinson. Fast, automated, N-dimensional phase-unwrapping algorithm. *Magnetic Resonance in Medicine*, 49(1):193–197, 2003.
 18. Mark Jenkinson, Christian F. Beckmann, Timothy E.J. Behrens, Mark W. Woolrich, and Stephen M. Smith. Fsl. *NeuroImage*, 62(2):782–790, 2012. 20 YEARS OF fMRI.
 19. Woojin Jung, Steffen Bollmann, and Jongho Lee. Overview of quantitative susceptibility mapping using deep learning: Current status, challenges and opportunities. *NMR in Biomedicine*, n/a(n/a):e4292, 2020. e4292 NBM-19-0283.R1.
 20. Youngwook Kee, Dong Zhou, Yi Wang, and Pascal Spincemaille. Preconditioned total field inversion (TFI) method for quantitative susceptibility mapping. *Magnetic resonance in medicine*, 78, 07 2016.
 21. Erich Kobler, Teresa Klatzer, Kerstin Hammernik, and Thomas Pock. "Variational Networks: Connecting Variational Methods and Deep Learning". In Volker Roth and Thomas Vetter, editors, *Pattern Recognition*, pages 281–293, Cham, 2017. Springer International Publishing.
 22. Kuo-Wei Lai, M. Aggarwal, P. V. Zijl, Xuezhe Li, and Jeremias Sulam. Learned proximal networks for quantitative susceptibility mapping. *Medical image computing and computer-assisted intervention : MICCAI International Conference on Medical Image Computing and Computer-Assisted Intervention*, 12262:125–135, 2020.
 23. Vera Lambrecht, Jannis Hanspach, Alana Hoffmann, Lisa Seyler, Angelika Mennecke, Sina Straub, Franz Marxreiter, Tobias Bäuerle, Frederik B. Laun, and Jürgen Winkler. Quantitative susceptibility mapping depicts severe myelin deficit and iron deposition in a transgenic model of multiple system atrophy. *Experimental Neurology*, 329:113314, 2020.
 24. Christian Langkammer, Kristian Bredies, Benedikt Poser, Markus Barth, Gernot Reishofer, Audrey Fan, Berkin Bilgic, Franz Fazekas, Caterina Mainero, and Stefan Ropele. Fast quantitative susceptibility mapping using 3D EPI and total generalized variation. *NeuroImage*, 111, 02 2015.
 25. Christian Langkammer, Lukas Pirpamer, Stephan Seiler, Andreas Deistung, Ferdinand Schweser, Sebastian Franthal, Nina Homayoon, Petra Katschnig-Winter, Mariella Koegl-Wallner, Tamara Pendl, Eva Maria Stoegerer, Karoline Wenzel, Franz Fazekas, Stefan Ropele, Jürgen Rainer Reichenbach, Reinhold Schmidt, and Petra Schwingenschuh. Quantitative Susceptibility Mapping in Parkinson's Disease. *PLOS ONE*, 11(9):1–13, 09 2016.
 26. Christian Langkammer, Ferdinand Schweser, Nikolaus Krebs, Andreas Deistung, Walter Goessler, Eva Scheurer, Karsten Sommer, Gernot Reishofer, Kathrin Yen, Franz Fazekas, Stefan Ropele, and Jürgen Reichenbach. Quantitative susceptibility mapping (QSM) as a means to measure brain iron? A post mortem validation study. *NeuroImage*, 62:1593–9, 05 2012.
 27. Wei Li, Bing Wu, and Chunlei Liu. Quantitative Susceptibility Mapping of Human Brain Reflects Spatial Variation in Tissue Composition. *NeuroImage*, 55:1645–56, 04 2011.
 28. Juan Liu and K. Koch. Deep quantitative susceptibility mapping for background field removal and total field inversion. *arXiv: Medical Physics*, 2019.
 29. Juan Liu and Kevin M. Koch. "Deep Gated Convolutional Neural Network for QSM Background Field Removal". In Dinggang Shen, Tianming Liu, Terry M. Peters, Lawrence H. Staib, Caroline Essert, Sean Zhou, Pew-Thian Yap, and Ali

- Khan, editors, *Medical Image Computing and Computer Assisted Intervention – MICCAI 2019*, pages 83–91, Cham, 2019. Springer International Publishing.
30. Tian Liu, Jing Liu, Ludovic Rochefort, Pascal Spincemaille, Ildar Khalidov, James Ledoux, and Yi Wang. Morphology Enabled Dipole Inversion (MEDI) from a Single-Angle Acquisition: Comparison with COSMOS in Human Brain Imaging. *Magnetic resonance in medicine : official journal of the Society of Magnetic Resonance in Medicine / Society of Magnetic Resonance in Medicine*, 66:777–83, 09 2011.
 31. Tian Liu, Pascal Spincemaille, Ludovic Rochefort, Bryan Kressler, and Yi Wang. Calculation of susceptibility through multiple orientation sampling (COSMOS): A method for conditioning the inverse problem from measured magnetic field map to susceptibility source image in MRI. *Magnetic resonance in medicine : official journal of the Society of Magnetic Resonance in Medicine / Society of Magnetic Resonance in Medicine*, 61:196–204, 01 2009.
 32. Tian Liu, Krishna Surapaneni, Min Lou, Liuquan Cheng, Pascal Spincemaille, and Yi Wang. Cerebral Microbleeds: Burden Assessment by Using Quantitative Susceptibility Mapping. *Radiology*, 262:269–78, 11 2011.
 33. José P. Marques, Tobias Kober, Gunnar Krueger, Wietske van der Zwaag, Pierre-François Van de Moortele, and Rolf Gruetter. Mp2rage, a self bias-field corrected sequence for improved segmentation and t1-mapping at high field. *NeuroImage*, 49(2):1271–1281, 2010.
 34. José P. Marques, Jakob Meineke, Carlos Milovic, Berkin Bilgic, Kwok-Shing Chan, Renaud Hedouin, Wietske van der Zwaag, Christian Langkammer, and Ferdinand Schweser. Qsm reconstruction challenge 2.0: A realistic in silico head phantom for mri data simulation and evaluation of susceptibility mapping procedures. *Magnetic Resonance in Medicine*, 86(1):526–542, 2021.
 35. Carlos Milovic, Cristian Tejos, Julio Acosta-Cabronero, Pinar Senay Özbay, Ferdinand Schweser, Jose Pedro Marques, Pablo Irarrazaval, Berkin Bilgic, and Christian Langkammer. The 2016 QSM Challenge: Lessons learned and considerations for a future challenge design. *Magnetic Resonance in Medicine*, 84(3):1624–1637, 2020.
 36. Stanley Osher, Wotao Yin, Donald Goldfarb, and Jinjun Xu. An Iterative Regularization Method for Total Variation-Based Image Restoration. *Multiscale Modeling and Simulation Journal*, 4, 01 2005.
 37. Simon Daniel Robinson, Barbara Dymerska, Wolfgang Bogner, Markus Barth, Olga Zanic, Sigrun Goluch, Günther Grabner, Xenia Deligianni, Oliver Bieri, and Siegfried Trattnig. Combining phase images from array coils using a short echo time reference scan (composer). *Magnetic Resonance in Medicine*, 77(1):318–327, 2017.
 38. Olaf Ronneberger, Philipp Fischer, and Thomas Brox. U-Net: Convolutional Networks for Biomedical Image Segmentation. *CoRR*, abs/1505.04597, 2015.
 39. Olga Russakovsky, Jia Deng, Hao Su, Jonathan Krause, Sanjeev Satheesh, Sean Ma, Zhiheng Huang, Andrej Karpathy, Aditya Khosla, Michael S. Bernstein, Alexander C. Berg, and Fei-Fei Li. ImageNet Large Scale Visual Recognition Challenge. *CoRR*, abs/1409.0575, 2014.
 40. Rares Salomir, Baudouin Denis de Senneville, and Chrit TW Moonen. A fast calculation method for magnetic field inhomogeneity due to an arbitrary distribution of bulk susceptibility. *Concepts in Magnetic Resonance Part B: Magnetic Resonance Engineering*, 19B(1):26–34, 2003.
 41. Marvin A. Schofield and Yimei Zhu. Fast phase unwrapping algorithm for interferometric applications. *Opt. Lett.*, 28(14):1194–1196, Jul 2003.

42. Ferdinand Schweser, Andreas Deistung, Berengar W. Lehr, and Jürgen R. Reichenbach. Differentiation between diamagnetic and paramagnetic cerebral lesions based on magnetic susceptibility mapping. *Medical Physics*, 37(10):5165–5178, 2010.
43. Ferdinand Schweser, Andreas Deistung, Berengar Wendel Lehr, and Jürgen Rainer Reichenbach. Quantitative imaging of intrinsic magnetic tissue properties using MRI signal phase: An approach to in vivo brain iron metabolism? *NeuroImage*, 54(4):2789–2807, 2011.
44. Ferdinand Schweser, Andreas Deistung, and Jürgen Reichenbach. Foundations of MRI phase imaging and processing for Quantitative Susceptibility Mapping (QSM). *Zeitschrift für medizinische Physik*, 26, 12 2015.
45. Ferdinand Schweser, Andreas Deistung, Karsten Sommer, and Jürgen Rainer Reichenbach. Toward online reconstruction of quantitative susceptibility maps: Superfast dipole inversion. *Magnetic resonance in medicine*, 69(6):1581–1593, 2013.
46. Karin Shmueli, Jacco de Zwart, Peter Gelderen, Tie-Qiang Li, Stephen Dodd, and Jeff Duyn. Magnetic susceptibility mapping of brain tissue in vivo using mri phase data. *Magnetic resonance in medicine : official journal of the Society of Magnetic Resonance in Medicine / Society of Magnetic Resonance in Medicine*, 62:1510–22, 12 2009.
47. Hongfu Sun and Alan H. Wilman. Background field removal using spherical mean value filtering and Tikhonov regularization. *Magnetic Resonance in Medicine*, 71(3):1151–1157, 2014.
48. J.M.G. van Bergen, J. Hua, P.G. Unschuld, I.A.L. Lim, C.K. Jones, R.L. Margolis, C.A. Ross, P.C.M. van Zijl, and X. Li. Quantitative Susceptibility Mapping Suggests Altered Brain Iron in Premanifest Huntington Disease. *American Journal of Neuroradiology*, 37(5):789–796, 2016.
49. Yi Wang, Pascal Spincemaille, Zhe Liu, Alexey Dimov, Kofi Deh, Jianqi Li, Yan Zhang, Yihao Yao, Kelly Gillen, Alan Wilman, Ajay Gupta, Apostolos Tsiouris, Ihami Kovanlikaya, Gloria Chiang, Jonathan Weinsaft, Lawrence Tanenbaum, Weiwei Chen, Wenzhen Zhu, Shixin Chang, and Martin Prince. Clinical quantitative susceptibility mapping (QSM): Biometal imaging and its emerging roles in patient care: Clinical QSM Biometals. *Journal of Magnetic Resonance Imaging*, 46, 03 2017.
50. Hongjiang Wei, Steven Cao, Yuyao Zhang, Xiaojun Guan, Fuhua Yan, Kristen Yeom, and Chunlei Liu. Learning-based single-step quantitative susceptibility mapping reconstruction without brain extraction. *NeuroImage*, 202:116064, 08 2019.
51. Sam Wharton and Richard Bowtell. Whole-brain susceptibility mapping at high field: A comparison of multiple- and single-orientation methods. *NeuroImage*, 53:515–25, 11 2010.
52. Sam Wharton, Andreas Schäfer, and Richard Bowtell. Susceptibility Mapping in the Human Brain Using Threshold-Based k-Space Division. *Magnetic resonance in medicine : official journal of the Society of Magnetic Resonance in Medicine / Society of Magnetic Resonance in Medicine*, 63:1292–304, 05 2010.
53. Samuel Wharton and Richard Bowtell. Effects of white matter microstructure on phase and susceptibility maps. *Magnetic Resonance in Medicine*, 73(3):1258–1269, 2015.
54. Cynthia Wisnieff, Sriram Ramanan, John Olesik, Susan Gauthier, Yi Wang, and David Pitt. Quantitative susceptibility mapping (QSM) of white matter multiple sclerosis lesions: Interpreting positive susceptibility and the presence of iron. *Magnetic Resonance in Medicine*, 74(2):564–570, 2015.

55. Zhe Wu, Hongjian He, Yi Sun, Yiping Du, and Jianhui Zhong. High resolution myelin water imaging incorporating local tissue susceptibility analysis. *Magnetic Resonance Imaging*, 42, 06 2017.
56. Bing Xu, Naiyan Wang, Tianqi Chen, and Mu Li. Empirical evaluation of rectified activations in convolutional network, 2015.
57. Bing Yao, Tie-Qiang Li, Peter Gelderen, Karin Shmueli, Jacco de Zwart, and Jeff Duyn. Susceptibility Contrast in High Field MRI of Human Brain as a Function of Tissue Iron Content. *NeuroImage*, 62:1259–1266, 02 2009.
58. Jaeyeon Yoon, Enhao Gong, Itthi Chatnuntawech, Berkin Bilgic, Jingu Lee, Woojin Jung, Jingyu Ko, Hosan Jung, Kawin Setsompop, Greg Zaharchuk, Eung Yeop Kim, John Pauly, and Jongho Lee. Quantitative susceptibility mapping using deep neural network: QSMnet. *NeuroImage*, 179:199–206, 2018.
59. Jinwei Zhang, Zhe Liu, Shun Zhang, Hang Zhang, Pascal Spincemaille, Thanh D. Nguyen, Mert R. Sabuncu, and Yi Wang. Fidelity imposed network edit (FINE) for solving ill-posed image reconstruction. *NeuroImage*, January 2020.
60. Yan Zhang, Susan Gauthier, Ajay Gupta, Joseph Comunale, Gloria Chiang, Dong Zhou, Weiwei Chen, Ashley Giambrone, Wenzhen Zhu, and Yi Wang. Longitudinal change in magnetic susceptibility of new enhanced multiple sclerosis (MS) lesions measured on serial quantitative susceptibility mapping (QSM). *Journal of magnetic resonance imaging : JMRI*, 44, 01 2016.
61. Dong Zhou, Tian Liu, Pascal Spincemaille, and Yi Wang. Background field removal by solving the Laplacian boundary value problem. *NMR in Biomedicine*, 27(3):312–319, 2014.
62. Pinar Senay Özbay, Andreas Deistung, Xiang Feng, Daniel Nanz, Jürgen Rainer Reichenbach, and Ferdinand Schweser. A comprehensive numerical analysis of background phase correction with V-SHARP. *NMR in Biomedicine*, 30(4):e3550, 2017. e3550 NBM-15-0276.R2.